

Quantum annealing eigensolver as a NISQ era tool for probing strong correlation effects in quantum chemistry

Aashna Anil Zade,^{1,2,*} Kenji Sugisaki,^{1,3,4,5} Matthias Werner,^{6,7,8} Ana Palacios,^{6,7,8} Jordi Riu,^{6,9} Jan Nogué,^{6,9} Artur Garcia-Saez,^{6,10} Arnau Riera,⁶ and V. S. Prasanna^{1,11,†}

¹Centre for Quantum Engineering, Research and Education, TCG CREST, Kolkata 700091, India

²Department of Physics, IIT Tirupati, Chindapalle, Andhra Pradesh 517619, India

³Graduate School of Science and Technology, Keio University,

7-1 Shinkawasaki, Saiwai-ku, Kawasaki, Kanagawa 212-0032, Japan

⁴Quantum Computing Center, Keio University, 3-14-1 Hiyoshi, Kohoku-ku, Yokohama, Kanagawa 223-8522, Japan

⁵Keio University Sustainable Quantum Artificial Intelligence Center (KSQAIC), Keio University, 2-15-45 Mita, Minato-ku, Tokyo 108-8345, Japan

⁶Qilimanjaro Quantum Tech, Carrer de Vençuela 74, 08019 Barcelona, Spain

⁷Departament de Física Quàntica i Astrofísica, Facultat de Física, Universitat de Barcelona, 08028 Barcelona, Spain

⁸Institut de Ciències del Cosmos, Universitat de Barcelona, ICCUB, Martí i Franquès 1, 08028 Barcelona, Spain

⁹Universitat Politècnica de Catalunya, Carrer de Jordi Girona, 3, 08034 Barcelona, Spain

¹⁰Barcelona Supercomputing Center, Pl. Eusebi Güell 1, 08032 Barcelona, Spain

¹¹Academy of Scientific and Innovative Research (AcSIR), Ghaziabad 201002, India

(Dated: June 10, 2025)

The quantum-classical hybrid variational quantum eigensolver (VQE) algorithm is arguably the most popular noisy intermediate-scale quantum (NISQ) era approach to quantum chemistry. We consider the underexplored quantum annealing eigensolver (QAE) algorithm as a worthy alternative. We use a combination of numerical calculations for a system where strong correlation effects dominate, and conclusions drawn from our preliminary scaling analysis for QAE and VQE to make the case for QAE as a NISQ era contender to VQE for quantum chemistry. For the former, we pick the representative example of computing avoided crossings in the H_4 molecule in a rectangular geometry, and demonstrate that we obtain results to within about 1.2% of the full configuration interaction value on the D-Wave Advantage system 4.1 hardware. We carry out analyses on the effect of the number of shots, anneal time, and the choice of Lagrange multiplier on our obtained results. Following our numerical results, we carry out a detailed yet preliminary analysis of the scaling behaviours of both the QAE and the VQE algorithms to assess the competency of the former for NISQ era chemistry.

CONTENTS		B. VQE results for ground state energies	8
I. Introduction	2	IV. Comparison between scaling behaviours of QAE and VQE	9
II. Theory and Methodology	3	1. Problem inputs	10
A. Quantum annealing	3	2. The main processing steps	12
B. The QAE algorithm: a primer	3	3. Embedding	14
C. Avoided crossings	4	4. Net scaling behaviours	14
D. Computational details	5	V. Conclusion and future outlook	15
III. Results and Discussions	5	Acknowledgments	16
A. QAE results for avoided crossings	5	VI. Data availability	16
		References	16

* aashnazade@gmail.com

† srinivasaprasanna@gmail.com

A. Derivation of fidelity bounds	18
B. Cost of evaluating CISD Hamiltonian matrix elements	18
C. Details of input state preparation: a representative example	19

I. INTRODUCTION

The Variational Quantum Eigensolver (VQE) algorithm is the most well-known and arguably the most widely used NISQ era approach to quantum chemistry. Several works in literature have employed the algorithm, both on quantum hardware (for example, see Refs. [1–7] and simulation fronts (Refs. [8–15]). However, in gate-based NISQ hardware, noise poses significant problems, and thus obtaining results of high quality using VQE (or for that matter, any other gate-based algorithm applied to chemistry) is extremely challenging. On the other hand, on the quantum annealing front, the Quantum Annealer Eigensolver (QAE) [16], which is also a NISQ era quantum-classical hybrid approach and which is also built on the variational principle, has proven to yield highly accurate results [17]. Furthermore, due to its general purpose nature, QAE has been widely applied to a variety of problems. They include molecular vibrational spectra [16], complex eigenvalue problems [18], energy calculations for molecular electronic states [19, 20], relativistic calculations of fine structure splitting in highly charged atomic ions [17], simulating particle physics [21], and lattice gauge theories [22]. However, despite its general scope and better resilience to noise, the QAE algorithm has been vastly underexplored relative to VQE.

The versatility and robustness of QAE to quantum hardware errors as well as dearth in the range of applications in the context of quantum chemistry naturally prompts further exploration of obtaining molecular properties using the algorithm. In particular, it is interesting and timely to study the performance of QAE in domains where predicting strong correlation effects, one of the cornerstones of quantum many-body theoretic calculations applied to quantum chemistry, are at play. This would be a step towards mirroring the tremendous efforts that have been dedicated towards capturing strong correlation effects in the VQE framework [23–28].

While other quantum annealing algorithms for quantum chemistry do exist, such as the Xia–Bian–Kais (XBK) transformation [29, 30] and the Qubit Coupled Cluster (QCC) [31, 32] method, they have practical limitations. For instance, the XBK approach incurs a significant

qubit overhead due to the need to encode a k -local electronic structure Hamiltonian (initially represented as a weighted sum of tensor product of all Pauli operators) into a form involving only Pauli Z operators. The qubit count increases further due to quadratization required to transform it into a 2-local Ising Hamiltonian. In contrast, QAE minimises an energy functional expressed as a double sum over Hamiltonian matrix elements. Post encoding, this functional naturally results in a 2-local form compatible with the quantum annealer (see Eq. (4) below) thus avoiding the need for quadratization, the tradeoff here being that the encoded problem always exhibits a full connectivity among qubits. The QCC method on the other hand, although requiring fewer qubits than XBK [33], relies heavily on a classical optimizer to minimise the energy functional which can involve parameters scaling exponentially with the number of entanglers used to capture electron correlation [32]. Moreover, it was highlighted in [32] that the QCC method tends to exhibit the issue of convergence to different local minima. This problem is particularly severe for strongly correlated systems.

In this work, we begin by carrying out avoided crossings (AC) calculations on the well-known prototypical system: H_4 in a rectangular geometry [34], to showcase the strength of QAE in predicting physical effects in the strong correlation regime. We expand the many-body wave function in a basis of configuration state functions (CSFs) and recast the energy functional as an Ising Hamiltonian. We then determine the ground state energy and the excited state energy of interest to us using three approaches: quantum annealing (for which we employ the QAE algorithm; on the D-Wave Advantage machine), simulated annealing (for which we use simulated annealing eigensolver (SAE) approach), and the graphical unitary group approach full configuration interaction (GUGA-FCI; which we shall hereafter shorten to FCI for brevity) provided by GAMESS-US [35] for benchmarking our results. We also carry out an analysis of the ‘knobs’ of the QAE algorithm, such as the effect of the number of shots, the anneal time, and the choice of the Lagrange parameter on our AC results. For completeness, we also carry out VQE calculation for ground state energy estimation on the IBM superconducting devices.

Our numerical computations are followed by a preliminary analysis on the scaling behaviours of both the QAE and the VQE approaches (classical as well as quantum resources), with the goal of comparing the two. To that end, we consider the scaling of each of the steps of both the algorithms under some assumptions to arrive at the final scaling estimates.

The rest of the sections are organized as follows:

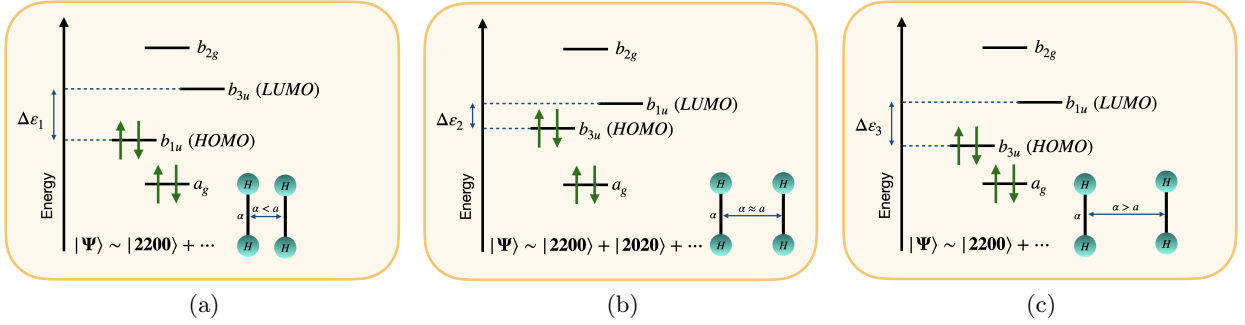


Figure 1: Molecular orbital diagram for H_4 across its potential energy curve, for the cases (a) $\alpha < a$, (b) $\alpha \approx a$, and (c) $\alpha > a$, where α denotes the distance between two H_2 sub-systems that constitute H_4 , whereas a is the bond length of the H_2 molecule. In the sub-figures, a_g , b_{1u} , etc refer to the irreducible representations of the D_{2h} point group, while $\Delta\epsilon_i$ is the difference in energy between the HOMO and LUMO across the PEC. HOMO and LUMO are the highest occupied and the lowest unoccupied molecular orbitals respectively.

Section II presents the relevant theory and methodology, while Section III discusses our findings from numerical calculations. In Section IV, we study the scaling behaviours of QAE and VQE, and conclude with Section V.

II. THEORY AND METHODOLOGY

A. Quantum annealing

Quantum annealing (QA) is a meta-heuristic that leverages quantum fluctuations, and is designed to solve computationally hard optimization problems, typically by encoding them into the ground state of a Hamiltonian [36–38]. QA involves preparing the ground state of an easily constructible Hamiltonian, H_I , which is typically chosen to be the transverse field Hamiltonian, and then gradually transforming it into another Hamiltonian, H_F , generally chosen to be the Ising Hamiltonian whose ground state encodes the solution to the problem. As one gradually goes from H_I to H_F according to $H(t) = \left(1 - \frac{t}{T}\right)H_I + \frac{t}{T}H_F$; $t \in [0, T]$, the system transitions smoothly from the ground state of H_I to the ground state of H_F . We add that while the adiabatic model described above is the theoretical model underlying QA, the latter, in practice, operates far from the adiabatic limit. In this work we use QAE [16] to map the electronic structure Hamiltonian, typically a k -local operator expressed as a weighted sum of Pauli strings, into an equivalent Ising form. We subsequently use QA to find its ground state.

B. The QAE algorithm: a primer

The QAE algorithm solves the eigenvalue equation $H|\Psi\rangle = E|\Psi\rangle$ by transforming it into an energy minimization problem. The energy functional considered is the expectation value of the Hamiltonian H with respect to an unknown state $|\Psi\rangle$. To avoid trivial solutions, the normalisation constraint $\langle\Psi|\Psi\rangle - 1 = 0$ is enforced by the inclusion of a Lagrange multiplier λ into the energy functional. The modified formulation after dropping the irrelevant constant is given by

$$\epsilon = \langle\Psi|H|\Psi\rangle - \lambda\langle\Psi|\Psi\rangle. \quad (1)$$

Assuming an ansatz of the form $|\Psi\rangle = \sum_{i=1}^{d_{CI}} c_i |\Phi_i\rangle$ where $\{|\Phi_i\rangle\}$ represent a set of d_{CI} known basis functions, the QAE algorithm aims to determine the unknown coefficients $\{c_i\}$ with $c_i \in [-1, 1]$ in the energy functional

$$\epsilon(\vec{c}, \lambda) = \sum_{i,j=1}^{d_{CI}} c_i c_j H_{ij} - \lambda \sum_{i=1}^{d_{CI}} c_i^2. \quad (2)$$

We subsequently use the fixed point encoding scheme where each coefficient c_i is encoded using K qubits $q_K^i \in \{-1, 1\}$ in the following manner

$$c_i = \sum_{\alpha=1}^{K-1} 2^{\alpha-K} q_\alpha^i - q_K^i \quad (3)$$

This approach converts the problem from a continuous optimization over the variables $\{c_i\}$ to a discrete opti-

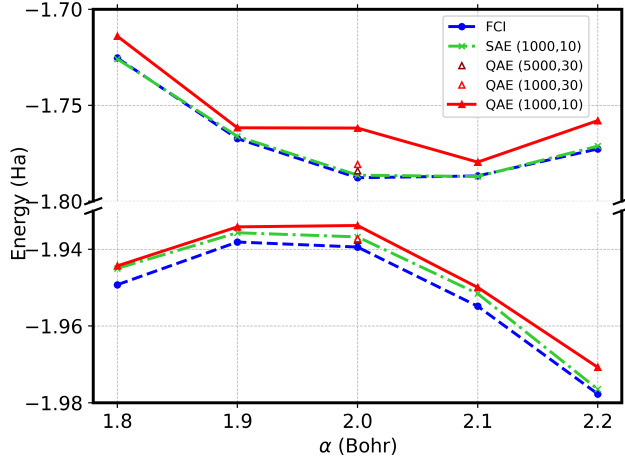


Figure 2: Comparison of the potential energy curves of the ground electronic state (singlet) and the first excited electronic state (singlet) obtained for H_4 for different values of α , using FCI, SAE, and QAE (on the D-Wave hardware). We calculate all of the data points with 1000 shots and 10 repetitions (denoted in the legend as (1000,10)), and setting an anneal time of 20 microseconds. The red and brown hollow triangle markers indicate our results obtained with 1000 shots and 30 repetitions (denoted in the legend as (1000,30)) and with 5000 shots and 30 repetitions (denoted in the legend as (5000,30)) respectively.

mization problem over the binary variables $\{q_i\}$ i.e.

$$\epsilon(\vec{q}, \lambda) = \sum_{i,j=1}^{d_{CI}} \left(\sum_{\alpha,\beta=1}^{K-1} 2^{\alpha+\beta-2K} q_{\alpha}^i q_{\beta}^j + 2^{\alpha+1-K} q_{\alpha}^i \pm 1 \right) (H_{ij} - \lambda \delta_{ij}) \quad (4)$$

making it suitable for implementation on current quantum annealers. In the above equation, $H_{ij} \equiv \langle \Phi_i | H | \Phi_j \rangle$ and δ_{ij} refers to the Kronecker delta function. The \pm sign arises from the product $q_K^i q_K^j$ which can be 1 or -1 . The pseudocode (see Algorithm 1) summarizes the QAE implementation employed.

In the succeeding paragraphs, we describe the theory behind avoided crossings, followed by details on obtaining them in the QAE framework.

Algorithm1 QAE

```

Get  $H$ , Guess  $\lambda_{\pm}$ 
for  $\lambda \in [\lambda_-, \lambda_+]$  do
   $\epsilon(\vec{q}, \lambda) \leftarrow \epsilon(\vec{c}, \lambda)$  ▷ Encoding
   $\vec{q}_{\text{optimum}} \leftarrow [\epsilon(\vec{q}, \lambda)]_{\text{min}}$  ▷ Annealing
   $\vec{c}_{\text{optimum}} \leftarrow \vec{q}_{\text{optimum}}$  ▷ Reverse encoding
   $E_{\lambda} \leftarrow \epsilon(\vec{c}_{\text{optimum}}, \lambda)$ 
end for
Get  $\min\{E_{\lambda}\}$ 

```

C. Avoided crossings

An accurate description of ground and excited state potential energy curves (PECs) in regions where the electronic states interact strongly poses a challenge for well-known electronic structure methods such as the single reference coupled cluster approach [39–42]. These strongly interacting regions, termed as avoided crossings, involve geometries far from equilibrium where an accurate description of the electronic structure requires accounting for both strong and weak correlation effects, of which the former are predominant. In fact, ACs are a key indicator of strong correlation effects wherein the Hartree–Fock (HF) state alone no longer acts as a good reference for methods such as coupled cluster to compute accurate wave functions.

In the case of H_4 , this behaviour originates from the quasi-degenerate nature of the molecular orbitals, which can be continuously varied by changing the parameter that defines the geometry, α . The parameter corresponds to the distance between the two H_2 sub-systems, each with bond distance separation given by a . Specifically, when $\alpha \neq a$, the energy gap between the highest occupied molecular orbital (HOMO) and the lowest unoccupied molecular orbital (LUMO) is substantial. This makes the HF configuration, given by $|2200\rangle$ in the occupancy number representation (specification of the occupancy of each orbital), dominant such that $|\Psi\rangle_{\alpha \neq a} \sim |2200\rangle$, thus enabling single reference methods to accurately describe the wave function in these regions. Conversely, when $\alpha \approx a$, the HOMO and LUMO become nearly degenerate and an additional configuration $|2020\rangle$ begins to contribute significantly alongside HF resulting in $|\Psi\rangle_{\alpha \approx a} \sim |2200\rangle - |2020\rangle$. Figure 1 depicts the orbital degeneracies along varying parameter values. The ‘ \sim ’ symbol is to indicate that we are ignoring the normalization constants for brevity, whereas the ‘ \dots ’ symbol indicates that the rest of the states besides those mentioned on the right hand side do not contribute significantly.

The AC in H_4 can also be understood from a group theoretic point of view. The non crossing rule put forth

by Neumann and Wigner in 1929 [43] states that PECs corresponding to electronic states of same point group symmetry do not cross. Formally symmetry of an electronic state can be determined by evaluating the direct product of the irreducible representation of each of the electrons involved in that state. For H_4 , this corresponds to the A_g symmetry of the D_{2h} point group.

ACs are significant in quantum chemistry for studying reaction dynamics. They often correspond to the energy of transition states in chemical reactions. By accurately determining the energy at an AC, we can identify the major reaction pathway among multiple possible transition states. In this work, we use QAE to predict ACs in the H_4 molecule. The primary source of avoided crossing arises from the symmetry of the electronic states. Additionally, this model system allows us to vary the degree of orbital quasi-degeneracies by simply changing the geometry defining parameter.

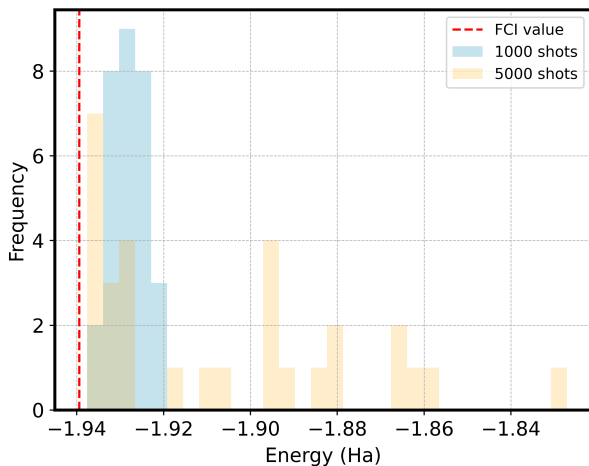


Figure 3: Comparison of the ground state energy at the AC geometry obtained by executing QAE (on the D-Wave hardware) with 1000 shots and 30 repetitions (marked in blue) and 5000 shots and 30 repetitions (marked in green). The reference FCI value is presented as a dashed line.

D. Computational details

We begin by detailing the input parameters associated with our chosen molecule. H_4 is a planar four-electron model consisting of two interacting hydrogen molecules. The geometry is defined by intermolecular and intramolecular H...H distances α and a respectively,

where the latter is fixed to 2 Bohr. We calculate the ground and excited state energies at five geometries ($\alpha = 1.8, 1.9, 2.0, 2.1,$ and 2.2 Bohr; for the purposes of this work, we fix the resolution to 0.1 Bohr in view of the cost of quantum computational resources). We work with the STO-3G minimal basis set and employ the D_{2h} point group symmetry in our calculations.

To generate the CI matrix elements, H_{ij} , we use the GUGA-FCI approach available in the GAMESS-US program [35]. There are 8 CSFs for our 4 electron 4 orbital active space. This corresponds to an 80×80 all-to-all connected QUBO problem with $K = 10$.

We now comment on the computational details in the QAE part of our workflow. We use the D-Wave Advantage system 4.1 for all the QAE computations. We need to choose a range of λ values across which we scan. For this purpose, we first carry out several SA computations, each with a different choice for the λ range. A given λ range is subdivided into 1000 parts, and for each of those λ values, we carry out SAE (the approach involves all of the steps from QAE, except that the quantum annealing is replaced by simulated annealing) with 1000 shots. We pick that λ range for our QAE calculation that gives the best energy value. All of our SAE calculations are performed using the D-Wave Ocean Toolkit [44]. For our QAE calculations, we subdivide the chosen λ range into 100 values, and perform QA with 1000 shots for each of those λ values. For each anneal, we pick the default anneal time of 20 microseconds. Once we find the lowest energy from the procedure, we repeat the process 10 times (we term this as 10 repetitions hereafter) and choose the lowest energy among the set of values for our final result for the ground state energy. We note that for an excited state calculation, we follow the same procedure, except that the Hamiltonian, H_e , is constructed from the ground state Hamiltonian, H_g , and the ground state wave function, $|\Psi_g\rangle$, by invoking the Brauer’s theorem as

$$H_e = H_g + S_0 |\Psi_g\rangle \langle \Psi_g|.$$

This theorem states that the lowest eigenvalue of H_e corresponds to the second-lowest eigenvalue of H_g , which represents the first excited state energy we are looking for. Here, $S_0 > E_e - E_g$. We choose S_0 to be 1 in our work.

III. RESULTS AND DISCUSSIONS

A. QAE results for avoided crossings

We now discuss our results. Figure 2 presents our results from annealing (with accompanying data provided in

Table I), where we compare the predicted avoided crossing from QAE with SAE and FCI, with 1000 shots and 10 repetitions. From the figure, we see that QAE, SAE, and FCI yield an energy difference (at the AC geometry, that is, 2 Bohr) of 0.17195, 0.15037, and 0.15169 Hartree (Ha) respectively. Thus, QAE is able to predict AC in the chosen system to within about 13 percent of the FCI value. The plot also shows that SAE is clearly in better agreement with the FCI values than QAE with both the ground and excited state energies at all of the geometries considered. A major bottleneck in QAE which is otherwise absent in SAE is the requirement for embedding. The QAE formulation results in a problem graph which is inherently fully connected regardless of the specific problem instance. Embedding thus refers to the process of mapping this fully connected graph onto sparsely connected qubits of the quantum annealer (here Pegasus topology [45] of D-Wave). This process incurs a significant qubit overhead and thus more error due to the increase of the search space (given by the physical Hilbert space dimension) while the logical solution space remains constant. SAE on the other hand is less error prone since classical computers are more robust to errors. Furthermore, the quality of the predicted excited state energy is relatively poor for the AC geometry using QAE (as we shall discuss later, the quality of results from QAE is still substantially better than those from a VQE computation with the same parameters). We can backtrack the performance of QAE to the several input parameters that go into obtaining a QAE result, such as (but not limited to) the number of shots and number of repetitions, anneal time, and choice of λ range. We devote the subsequent paragraphs to analyzing the effect of these three parameters on the AC results.

We begin by carrying out AC calculations with 1000 shots and 30 repetitions. As Figure 2 shows, increasing the number of repetitions drastically improves the quality of the excited state energy (the difference with respect to the FCI value) improves from 25.8 mHa to 7 mHa and improves the agreement of the ground state energy with the FCI value to 2.17 mHa (from 5.6 mHa). The AC value improves from 20.2 mHa for 10 repetitions to 2.6 mHa for 30 repetitions. We extend the analysis further by increasing the number of repetitions all the way to 100, but find that the AC value remains unchanged. Thus, we instead increase the number of shots to 5000 while keeping the number of repetitions fixed at 30. Figure 3 presents our findings, with the accompanying data given in Table I. The results indicate that as expected, one obtains better agreement with the FCI value for the AC with larger number of shots and repetitions. Furthermore, we see that the QAE result now is in much better agreement with the

Table I: Table presenting data (with 1000 shots and across 10 repetitions) on the percentage accuracies of the ground state (\mathcal{A}_g) and excited state energies (\mathcal{A}_e) as well as the avoided crossings (\mathcal{A}_{AC}) for the geometries considered for this work, all of them relative to their respective FCI values. The fourth row gives results with 1000 shots and 30 repetitions at the AC geometry, whereas the last row presents results with 5000 shots and across 30 repetitions (only at the AC geometry). The geometries are specified by α in units of Bohr. The entries shown in parentheses for the AC geometry indicates the difference between that energy and its FCI counterpart (in units of mHa).

Shots	α	\mathcal{A}_g	\mathcal{A}_e	\mathcal{A}_{AC}
	1.8	99.75	99.34	102.87
	1.9	99.80	99.68	100.98
1000	2.0	99.71 (5.6)	98.55 (25.8)	113.35 (20.2)
		99.89 (2.17)	99.61 (7.0)	103.20 (2.6)
	2.1	99.75	99.60	101.36
	2.2	99.65	99.17	103.81
5000	2.0	99.91 (1.83)	99.79 (3.67)	101.22 (1.85)

FCI value, differing only by 1.22 percent (5000 shots, 30 repetitions), as opposed to the 1000 shots 10 repetitions value of 13.35 percent and the 1000 shots 30 repetitions value of 3.2 percent. These percentages correspond to an energy difference ($E_{AC,FCI} - E_{AC,QAE}$) of 1.85 mHa, 20.2 mHa, and 2.6 mHa respectively. The values of AC obtained with 5000 shots and 30 repetitions, 1000 shots and 10 repetitions, and 1000 shots and 30 repetitions are 0.15354, 0.17195, and 0.15654 Ha respectively.

We turn our attention to Figure 4, where we plot the CI coefficients that we obtained from the ground state QAE calculation versus the coefficient index. We benchmark the computed CI coefficients employing QAE with those obtained from FCI. We carry out the exercise for both the 1000 and the 5000 shot cases, each with 30 repetitions. The purpose of the plot is to check the quality of the coefficients, which in turn indicates the quality of the predicted wave function. We see that the coefficients are all in reasonable agreement with their FCI counterparts. While the plot itself seems to yield almost similar set of coefficients by using 5000 shots over 1000 shots, this seemingly insignificant difference between their results is reflected in the subsequent ground state energy calculations as seen in the preceding paragraphs. Unsurprisingly, we also see the chemistry at play, where two coefficients are almost equally important (unlike the single reference scenario where only the HF state dominates). We also check the fidelity as well as the difference between AC predicted

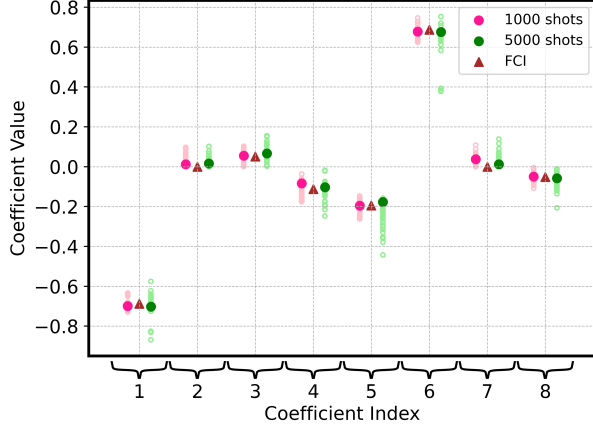
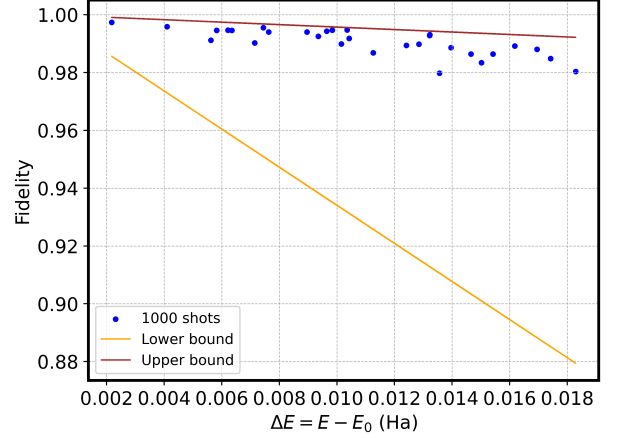
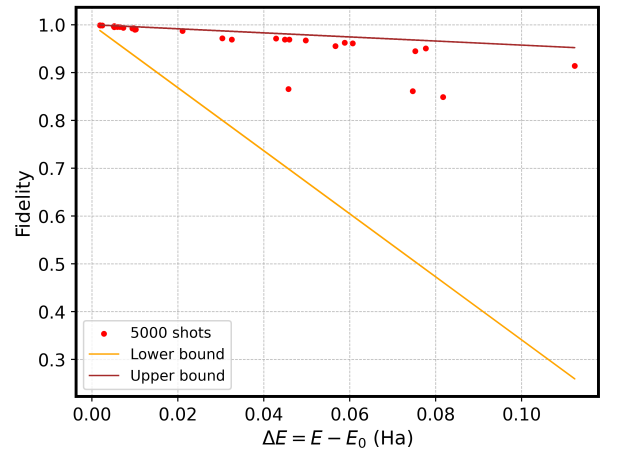


Figure 4: Comparison of configuration interaction coefficients for the ground state obtained using QAE with exact values of the coefficients from FCI (denoted as a brown triangle) for 1000 and 5000 shots, both with 30 repetitions, at the AC geometry. Each of the pink (1000 shots) and green (5000 shots) circles denotes the result from a repetition.

using QAE and FCI, and find them to be 99.735% and 2.6 mHa respectively for QAE calculation with 1000 shots and 30 repetitions, whereas they improve to 99.886% and 1.85 mHa respectively when we employ 5000 shots and 30 repetitions. Figures 5(a) and (b) presents scatter plots between fidelity (\mathcal{F}) and ΔE , the difference between the QAE and the FCI ground state energy results. The fidelity is given by $|\langle \Psi_{QAE} | \Psi_{FCI} \rangle|^2$, where $|\Psi_{QAE}\rangle$ is the wave function constructed using the CI coefficients that QAE outputs, while $|\Psi_{FCI}\rangle$ refers to the FCI wave function. We observe from Fig. 5(a) (which has been plotted for the 1000 shots case) and (b) (the 5000 shots case) that our data unsurprisingly respects the bounds for fidelity, given by $1 - \frac{E_{g,QAE} - E_{g,FCI}}{E_{e,FCI} - E_{g,FCI}} \leq \mathcal{F} \leq 1 - \frac{E_{g,QAE} - E_{g,FCI}}{E_{max,FCI} - E_{g,FCI}}$, where $E_{g,FCI}$ and $E_{g,QAE}$ are the ground state energies calculated using FCI and QAE respectively, whereas $E_{e,FCI}$ and $E_{max,FCI}$ refer to the excited state of interest to our AC problem and maximum eigenvalue of H obtained from FCI. For the derivation of the bound, please see Appendix A. Our results also show that most of the data points are saturating the upper bound which means a majority of the population is contained in the ground state. Furthermore, we carry out linear regression analysis on our two data sets, and find that the Pearson coefficient, R , is anti-correlated at -0.84 for the 1000 shots case and -1.04 in the 5000 shots case. Ideally, we would expect that as we supply more shots, the strength of anti-



(a)



(b)

Figure 5: Scatter plots involving fidelity and ΔE values, for 1000 shots (sub-figure (a)) and 5000 shots (sub-figure (b)) cases. The former quantity refers to $|\langle \Psi_{QAE} | \Psi_{FCI} \rangle|^2$, where $|\Psi_{QAE}\rangle$ is the wave function constructed out of the CI coefficients obtained using QAE and $|\Psi_{FCI}\rangle$ is the FCI wave function. On the other hand, the latter is the difference between the QAE and the FCI ground state energy results.

correlation between the two quantities, \mathcal{F} and ΔE , would increase, based on the bounds seen earlier. Not surprisingly, we also find that the best-case fidelities and ground state energies that we obtain using QAE for both the 1000 and the 5000 shots cases (99.735% and 99.886% respectively) obey the aforementioned inequality relation.

We now comment on the effect of anneal time on our results. We begin by recalling that the Hamiltonian changes for the ground and excited states, and thus our assump-

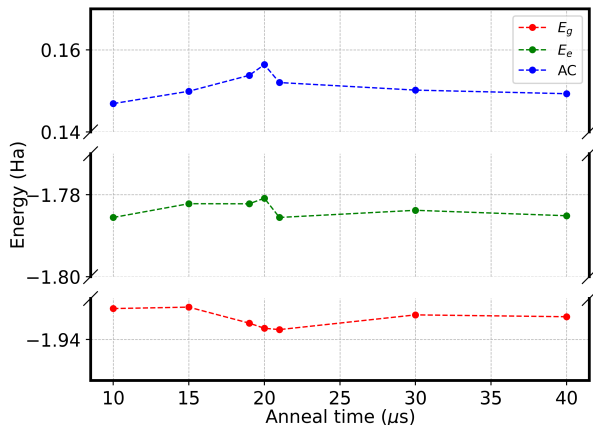


Figure 6: Plot showing the ground state energy (E_g), excited state energy (E_e), and avoided crossing (AC) values for different anneal times (in microseconds). The calculations are carried out with 1000 shots and 10 repetitions.

tion of setting the same anneal time for the ground and excited state computations is simplistic. Figure 6 presents our results for the variation of the ground state energy E_g , the excited state energy E_e , and AC with anneal time, with the purpose of going beyond the assumption that we had made in our main results shown in Figure 2. We choose to carry out the study with anneal times chosen between 10 and 40 microseconds. We carry out a coarse grained analysis in the interest of computational cost, and with unequal time resolutions across this range so that we probe with smaller resolution in and around the default anneal time of 20 microseconds. We use 1000 shots and 10 repetitions for the analysis. The plot shows that the default time happens to yield particularly poor results for the excited state relative to the other values of anneal time. If we instead pick the anneal times that give the best results for the ground state and excited state energies, the AC value improves from 0.17195 Ha to 0.15201 Ha. In the interest of computational cost, we did not carry out the analysis for the case of 5000 shots and 30 repetitions, but we anticipate to obtain further improvement in the AC energy value with this approach.

Finally, we focus on the choice of λ range for the problem. As mentioned in an earlier paragraph in Section II, we picked the λ range that gave the best SAE result. For the purposes of this work, we pick a range of 0.1 Ha. However, since SAE and QAE are different approaches to search for a desired solution, we pick three such ranges of 0.1 Ha each: a range containing the HF value (-1.77677 Ha), which is -1.8 to -1.7 Ha, one that is immediately

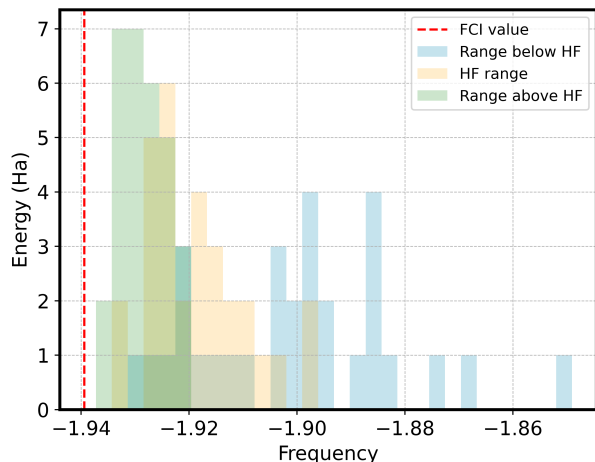


Figure 7: Comparison of the ground state energy across the three different λ ranges considered. The FCI value of the ground state energy is provided for reference as a dashed line.

below and another that is immediately above it. We term the three ranges as A, B, and C respectively. We note that the range we picked for our main calculations was the one immediately *above* the HF value, that is, range C. Figure 7 presents our results justifying this choice. We observe that our choice of λ range from SAE calculations were sufficiently good within a calculation involving 30 repetitions.

B. VQE results for ground state energies

For our VQE calculations, we only consider the ground state energy, although it is possible in principle to obtain the excited state energy of interest, using an equation of motion based VQE approach. QAE naturally incorporates CI allowing it to accurately predict energies both near equilibrium and at far-from-equilibrium geometries, effectively capturing both weak and strong correlation effects. In contrast, VQE with the UCCSD ansatz works best for near-equilibrium geometries and is unable to account for strong correlation effects. A fair comparison with QAE would require that we employ a multi-reference theory, for example, the icMRUCC (internally contracted multi-reference unitary coupled cluster) [46], where the reference state is a linear combination of multiple determinants. However, pursuing a multi-reference treatment poses certain challenges. First, one must survey the class of multi-reference theories and identify the one that is best

suites for VQE in terms of cost of implementation. Furthermore, in multi-reference theories where redundancies are not naturally accounted for, the computational cost to remove redundancies (duplicate states that need to be removed) is not necessarily easy. For example, in the icM-RUCC theory, the process of obtaining the indices for the linearly independent excitation amplitudes involves computing square root of an overlap matrix, which is computationally hard for large matrices.

Given the current limitations in two-qubit gate fidelities, we implement only a single-parameter VQE using the UCCSD ansatz, focusing on measuring only the dominant terms in the Hamiltonian. To capture correlation energy effectively in a multi-reference approach, we would need to measure at least two dominant terms from the Hamiltonian. Consequently, the multi-reference theory requires more resources. Thus, our UCCSD results serve as an upper bound to the values obtained from a multi-reference UCCSD approach, which, if implemented on a quantum computer with improved gate fidelities, would yield better quality results for the ground state energy than UCCSD in strongly correlated regimes.

We carry out our 26-parameter VQE-UCCSD calculation on the `ibm_kiev` device. The choice of hardware was made by comparing the CLOPS for the three currently available quantum computers (Brisbane, Sherbrooke, and Kyiv), and picking the one with the highest CLOPS. All of our calculations were performed with 4096 shots, and we quote our result by averaging over 10 repetitions. We begin by specifying the system parameters: processor type: Eagle R3, native gates: {ECR, ID, RZ, SX, X}, median ECR error: 1.086×10^{-2} , median readout error: 1.367×10^{-2} , median T1: 289.88 μ s, median T2: 113.13 μ s, and connectivity: heavy hexagonal lattice topology. We incur 1716 ECR gates (the number of one-qubit gates are 16500, 5844, and 1444 for RZ, SX, and X respectively). We note that even if the device had been fully connected, \mathcal{N}_{2qg} is still 1440, which would yield a rather low result fidelity. For example, assuming an optimistic estimate of 0.999 for the two-qubit gate fidelity (for comparison, state-of-the-art commercial quantum computers such as the IonQ Forte-I have current fidelities hovering in and around 0.99), an estimate of the result fidelity even with a fictitious all-to-all connected topology is a mere $\sim 0.999^{1440} \approx 0.2$. Thus, in order to obtain meaningful results, one needs to aggressively optimize the quantum circuit in addition to implementing additional resource reduction strategies to reduce the number of measurements, etc [15]. The authors of the cited work show that with a suite of such classically resource-intensive strategies, the number of gates can be reduced to the extent that makes computation on current-day quantum devices

possible. We borrow their techniques for our computations, and briefly describe them below before delving into our findings from the computations themselves. We begin by carrying out a VQE calculation on a traditional computer. We then carry out optimization on two fronts: wave function (the quantum circuit itself) and Hamiltonian (reducing the number of terms in the Hamiltonian, so that the number of circuits evaluated is reduced). On the circuit optimization side, we first pass our quantum circuit with the optimal parameters into three optimization routines sequentially: Qiskit ($L = 3$) [47], Pytket [48], and PyZX [49]. This was followed by an additional layer of circuit optimization using reinforcement learning-based ZX calculus routine and a causal flow preserving ZX calculus module [50], followed by another round of Qiskit ($L = 3$) optimization to yield a quantum circuit with the following gate count: RZ: 38, SX: 19, X=11, and ECR: 12. On the Hamiltonian front, we group the Hamiltonian into cliques, which are sets of mutually (qubit-wise) commuting terms, and then group cliques that yield common energies into supercliques, based on ideas from Ref. [51]. We then pick the dominant superclique (in energy) for our hardware computation.

We measured two circuits (that belong to the two dominant supercliques) on the optimized quantum circuit built with optimized parameters to obtain the ground state energy. We find that in spite of reducing \mathcal{N}_{2qg} to 12, we obtain an energy of -1.71197 Ha (recalling that they were obtained by averaging over 10 repeats, each with 4096 shots), with a PFD of 7.81 percent relative to the value obtained in the same setting on a simulator (noiseless). It is also worth adding that the correlation energy itself in the noiseless setting is -0.08015 Ha, whereas the one predicted from the IBM execution is significantly different at 0.06480 Ha. Augmenting the computations with error mitigation techniques (outside the scope of the current work) can improve the quality of the result, but it is clear that in order to carry out more resource intensive MRUCC-VQE computations even in small active spaces such as the one we have chosen would require further advances on the hardware front. On the other hand, the QAE algorithm gives reasonable values for the ground state energy (-1.93760 Ha with 5000 shots and averaged over 30 repetitions) on the D-Wave hardware.

IV. COMPARISON BETWEEN SCALING BEHAVIOURS OF QAE AND VQE

In this section, we carry out a preliminary comparison of QAE and VQE, and wherever relevant, comment on scaling. Our analysis is preliminary in the following sense:

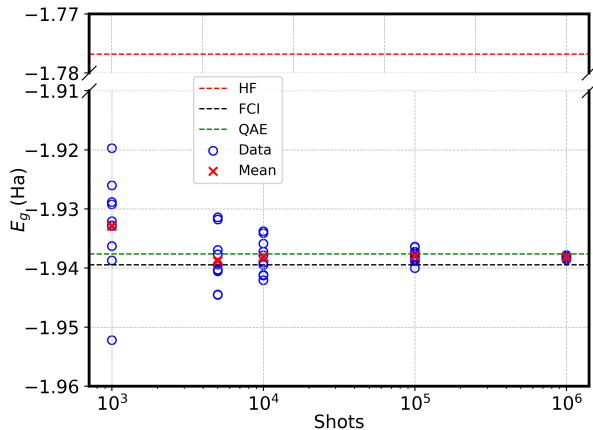


Figure 8: Comparison of the ground state energy (E_g) obtained using VQE across different number of shots. For each shot number, we repeat the VQE calculation 10 times (10 repetitions). The HF, the FCI, and the QAE (5000 shots and averaged over 30 repetitions) values are provided for reference.

We consider only the chemistry-inspired unitary coupled cluster ansatz and limited to the singles and doubles approximation (UCCSD) for VQE, and determinant-based configuration interaction in the singles and doubles approximation (CISD) for QAE (we use GUGA-based CI in our numerical calculations in the previous sections, but consider determinant-based CI for the scaling analysis on grounds of simplicity; as and when possible, we comment on GUGA-based CI). Furthermore, we do not compare QAE with variants of VQE, but with only the traditional version [1] of the latter. We also do not attempt to address in depth the open (yet critical) questions from both algorithms such as input state preparation in the case of VQE and anneal time scaling in the case of QAE. Figure 9 presents schematics of both the algorithms, where common numerical labels indicate points of comparison.

1. Problem inputs

- **One- and two- electron integrals:** Both QAE and VQE require us to supply one- and two- electron integrals. They are obtained from a classical computer, involving the HF (scales typically as N^4 for N spin-orbitals [52]) and atomic orbital to molecular orbital integral transformation (scales as N^5 [52]) steps. The number of Hamiltonian terms themselves scale as N^4 . This overhead can be re-

duced by employing techniques such as Hamiltonian factorization [53–55]. Reducing this overhead has the effect of reducing the number of circuit evaluations in VQE per iteration (since there are as many circuits per iteration as the number of Hamiltonian terms). On the other hand, in QAE, the ‘factorization’ needs to be performed on the wave function in order to reduce the number of the quantum annealing runs. In fact, the GUGA-based approach that we employ in this work corresponds to this procedure. The determinant-based wave function expansion is inefficient with respect to the number of variables, because Slater determinants are not necessarily spin eigenfunctions. Qualitatively, GUGA generates spin symmetry-adapted CSFs by block-diagonalizing the electron spin \mathbf{S}^2 operator to reduce the number of variables to optimize.

- **Evaluating Hamiltonian matrix elements:** Following the computation of integrals, the CI Hamiltonian matrix elements must be constructed classically prior to performing QAE. We therefore analyze the cost associated with such a construction. If there are d_{CI} coefficients, then noting that the Hamiltonian is hermitian, we need to evaluate $\frac{d_{CI}^2}{2} + \frac{d_{CI}}{2} \sim d_{CI}^2$ elements. We consider the CISD approximation for the purpose of the analysis. We also introduce some standard notation: n_o refers to the total number of occupied spin orbitals (i.e. total number of electrons), and n_v the number of unoccupied spin orbitals. A cursory look shows that since the number of matrix elements to evaluate goes as $n_o^4 n_v^4$ and the cost of constructing a CI matrix element, given the one- and two- electron integrals, by using the Slater–Condon rules goes at most as n_o^2 (corresponding to the case of the wavefunction in the bra and ket being the same), the cost of obtaining the CI Hamiltonian matrix elements is at most $n_o^6 n_v^4$, that is, N^{10} . However, this naive evaluation does not account for sparsity of the Hamiltonian (via the Slater–Condon rules) and also assumes that every matrix element evaluation is as costly as the costliest one’s evaluation. A more careful approach by accounting for the aforementioned considerations indicates a much cheaper scaling of N^6 . The details of the derivation are presented in Appendix B. The scaling behavior for evaluating matrix elements in GUGA-CI is very similar to that of determinant-based approach. However, GUGA-CI incurs an extra cost which comes from evaluating additional coefficients associated with pathways of the Shavitt graph, which can introduce an ex-

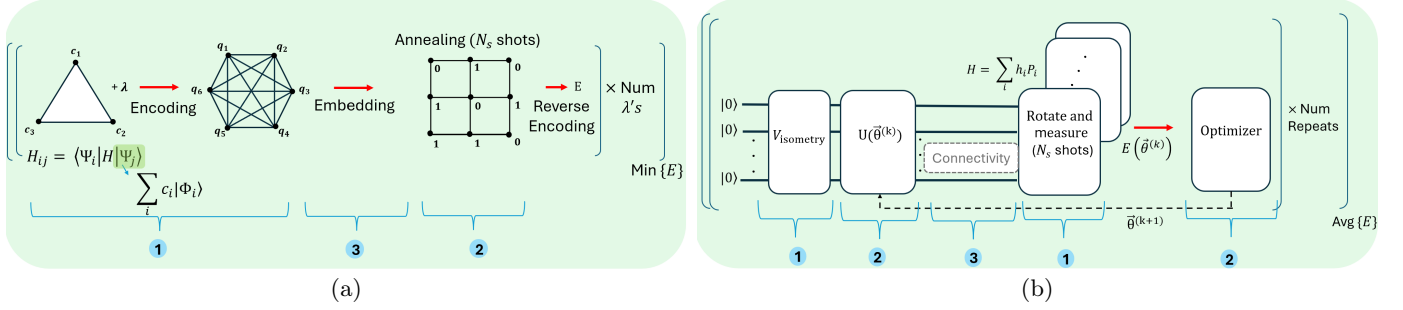


Figure 9: Schematic of the QAE (left panel) and the VQE (right panel) algorithms.

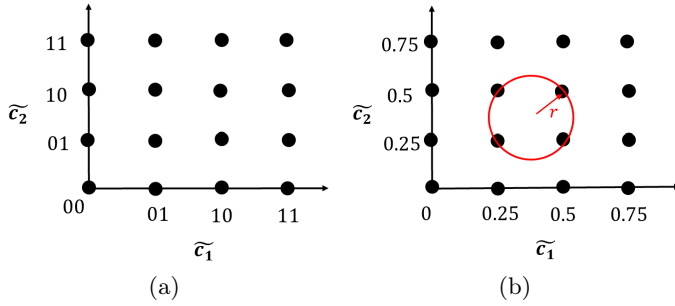


Figure 10: Optimisation domain for $N = 2$ and $K = 2$ in (a) the space of binary variables and (b) the space of real variables.

tra scaling of $\mathcal{O}(N)$. Therefore the overall computational cost for GUGA scales as $\mathcal{O}(N^7)$ [56, 57]. While the number of Hamiltonian matrix elements are fewer in GUGA-based CI than for determinant-based CI, the time taken to evaluate them can be longer for the former, due to evaluation of the aforementioned coefficients. Having discussed the cost of constructing the matrix elements, we now move onto analyzing the encoding cost of the energy functional in equation (2) to that given by equation (4).

- **Encoding in QAE in QUBO form:** We address the question of the scaling of the number of CI coefficients, c_i , as well as required scaling for the parameter, K .

- Although the number of coefficients in FCI scale as $d_{CI} \sim \binom{n_o}{m} \binom{n_v}{m} \sim \frac{n_o^m n_v^m}{(m!)^2}$, where m is the excitation level, one performs truncated CI calculations where m is fixed (for example, CISD, where $m = 2$), and thus the number of coefficients, in practice, scales polynomially as N^4 . We recall that K represents the number of

qubits used to discretise each coefficient such that the optimisation problem is over a set of binary variables. We qualitatively examine the scaling of K with the number of coefficients, d_{CI} . Each coefficient c_i is approximated by a K bit binary representation defined as

$$c_i \sim \tilde{c}_i = 0.c_{i1} \dots c_{ij} \dots c_{iK},$$

$$\forall j \text{ and each } i = 1, 2, \dots, d_{CI}$$

where $c_{ij} \in \{0, 1\}$ implying that each coefficient can take 2^K distinct values. This allows us to visualise the binary optimisation domain as an d_{CI} dimensional hyper-cube with each side consisting of 2^K discrete points. For simplicity we show the case for $d_{CI} = 2$ and $K = 2$ in Figure 10 (a). The resulting space is uniformly discretised with neighbouring points spaced $\frac{1}{2^K}$ distance apart. Furthermore, we consider a unit cell of this space, which is a hyper-cube of volume $\frac{1}{2^{Kd_{CI}}}$ and circumscribe it by a hyper-sphere, as seen in Figure 10(b). Thus, the discretization error is upper bounded by the radius of this hyper-sphere. Assuming equal discretization Δx in each dimension, we have

$$r^2 = \sum_{i=1}^{d_{CI}} \left(\frac{\Delta x}{2} \right)^2$$

$$r = \sqrt{d_{CI}} \frac{\Delta x}{2}$$
(5)

For constant error we demand $\sqrt{d_{CI}} \sim \frac{1}{\Delta x}$. Since $\Delta x = \frac{1}{2^K}$ we have

$$K \sim \log_2 d_{CI}$$
(6)

Therefore K must grow logarithmically with the number of coefficients, that is, as $\log_2 d_{CI}$

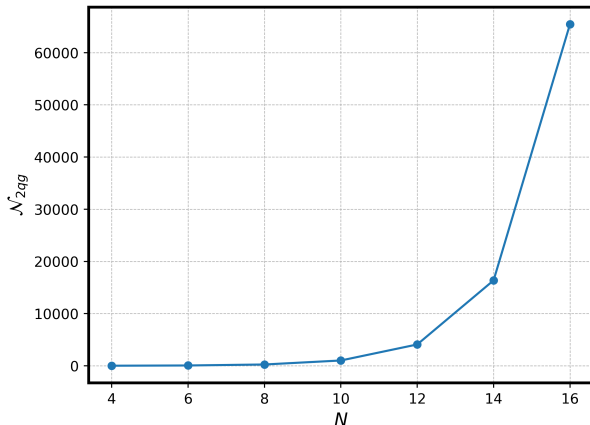


Figure 11: Figure illustrating the growth of the number of two qubit gates, \mathcal{N}_{2qg} , with number of qubits (written as N in the figure), for input state preparation in VQE.

which is equal to $\log_2 N^4$ for CISD. We now consider the corresponding cost in VQE, namely that for input state preparation via a quantum circuit.

- Input state preparation in VQE:** On the other hand, in VQE, one needs to construct the input reference state via an isometry, which in the case of a multi-reference UCC method, can be non-trivial. We note that not only does one need to employ classical many-body methods to find the coefficients of the entangled state, but also the cost of an input state preparation isometry in general scales exponentially in the number of two-qubit gates, \mathcal{N}_{2qg} [58]. Using chemical intuition to guess a small number of determinants (for instance, assuming a log log growth of the number of determinants in the number of all possible determinants) reduces the scaling ($\lceil \log(\log(2^N)) \rceil \sim \lceil \log(N) \rceil$), but the resulting circuits are still very deep for the NISQ era. We consider a toy example where we go from N of 4 to 16 in steps of 2, and thus the number of determinants for the input state would go from 2 to 4. We restrict the number of occupied spin-orbitals to 2, and find that \mathcal{N}_{2qg} increases as 2^N (the choice for coefficients is explained in Appendix C, while Figure 11 presents the result from our numerical analysis as a plot), in spite of a *loglog* reduction in the number of determinants (the worst case scaling for 2^N basis states is 4^N two-qubit gates [58, 59]). This unsurprising conclusion even for a limited toy example underscores the hardness of one of the biggest

open problems in gate-based algorithms: efficient input state preparation. Having said this, we also stress that our conclusions are drawn from numerical simulations that employ Qiskit’s isometry routines, and there are works in literature that attempt to address the topic of manual construction of polynomial-depth quantum circuits to prepare multi-configurational wave functions (for example, see Refs. [60] and [61]).

- The Lagrange multiplier:** In QAE, we need to select a range of λ values to scan, as well as the number of values in a selected range. This choice is not obvious, especially in light of the results shown in Figure 7, and we defer this analysis to a future study.

2. The main processing steps

For VQE, this corresponds to the cost function evaluation on a quantum computer and parameter updates on a classical computer. For QAE, this corresponds to the quantum annealing step.

- Choice of ansatz:** In VQE, the choice of ansatz is paramount to convergence. While physics-inspired/chemistry-based ansätze such as the UCC based ones yield excellent results in noiseless simulations, the entire class of hardware efficient ansätze often suffer from the notorious barren plateau problem [62]. On the other hand, we are unlikely to run into barren plateau issues in QAE, since by construction, we employ a CI wave function, which is physics-inspired/chemistry-based, and the algorithm involves an explore-exploit metaheuristic strategy, due to which we do not have a notion of iterations and convergence. It is worth adding that modified QAE workflows could have a convergence aspect to it, for example, see Ref. [17], but in our current study, we use the originally proposed QAE workflow, where we simply execute many shots of quantum annealing for each pre-selected λ value within a range.
- Number of two-qubit gates in ansatz:** A very important consideration is the absence of gates in QAE. Since gate errors are a major limiting factor in gate-based approaches of which VQE is one, the accuracy in results that one expects from a gate-based algorithm is usually limited, as opposed to approaches involving quantum annealing. The results from Ref. [17], where the authors achieve an

accuracy of about 99 percent, indeed reflects this observation. On the other hand, in VQE with the UCCSD ansatz for example, the number of two-qubit gates scale as $\sim N^5$. We can arrive at the estimate by considering that a Pauli gadget over N qubits (recalling that the number of spin-orbitals, N , is the number of qubits in VQE) scales at most linearly in N (assuming the Jordan–Wigner transformation), and that there are $n_o^2 n_v^2$ double excitations and thus as many Pauli words. The analysis assumes order one step one Trotterization. Thus, for example, even for a calculation involving a small molecule, where n_o and n_v are about 20 and 40 respectively, \mathcal{N}_{2qg} is already of the order of 100 million, and even with aggressive quantum circuit optimization strategies (for example, see Ref. [15]), it is unlikely to carry out such calculations at the physical qubit level on current and near-future quantum computers.

- **Initial guess for VQE parameters:** In VQE, we need to choose the initial guess for the parameters. Although we choose zeroes as initial guess values for our parameters, one can accelerate convergence by feeding in better-informed guesses such as MP2 (Møller–Plesset perturbation theory to second order in energy) initial guess (for example, see Ref. [6]). This, however, is accompanied by appropriate classical pre-processing steps.
- **Parameter update step in VQE:** In VQE, the parameter update limits prospects of achieving speed-up in large system sizes. For our numerical simulations whose results we will discuss in Section III B, we use the SLSQP optimizer, which is widely employed in literature. The cost function evaluation per iteration scales quadratically in the number of parameters (Refer section 2.2.4 in [63]). This implies the cost scales roughly as $\sim N^8$. However, since the scaling of the number of iterations with system size is highly problem-specific and non-trivial in nature, we defer the analysis to a future study.
- **Number of parameters to optimize:** This grows identically for both UCC-based VQE and QAE (which relies on CI). For example, in a UCCSD ansatz-based VQE computation, the number of parameters to be optimized grow as $n_o^2 n_v^2 \sim N^4$. However, it is important to also note that in the VQE-UCC framework, some higher-order excitations are accounted through the non-linear expansion of the UCC state, and the number of Slater determinants (or CSFs as in our case) included in the wave function expansion is larger for VQE-UCC than for QAE, even if the same number of parameters are included. For instance, even though UCCSD explicitly considers only T_1 and T_2 terms, it inherently includes correlation contributions from terms like $T_3, T_1^2, T_1^3, T_1^4, T_1 T_2$ etc. Therefore, while the number of parameters remain unchanged, the number of determinants involved is significantly larger in UCCSD compared to CISD.
- **Convergence:** This also leads us to the next point: since VQE is iterative in nature, the convergence behaviour heavily relies on the choice of optimizer (with the correct choice not being necessarily easy), the precision sought, as well as the nature of the specific system of interest. On the other hand, one can think of quantum annealing itself as performing the optimization in the case of QAE.
- We note that QAE possesses another inherent advantage in giving better results, since we pick the lowest energies across repetitions by construction. This is in contrast to VQE, where the mean expectation value across repetitions is typically chosen as the final result. This is because evaluating the expectation value of an observable A using VQE involves computing the weighted sum $\sum_i \lambda_i p_i$, where $\{\lambda_i\}$ are the eigenvalues of A . Here $p_i = \tilde{N}_i / N_s$ represents the probability of the state being in the i^{th} eigenstate, \tilde{N}_i denotes the number of shots yielding that eigenstate, and N_s is the total number of shots. Assuming the exact distribution has probabilities given by $p_i^0 = \tilde{N}_i^0 / N_s$, achieving an accurate estimate of the expectation value requires generating sufficient statistics such that $\tilde{N}_i \approx \tilde{N}_i^0, \forall i$. In contrast, in QAE, a single occurrence of the minimum energy is sufficient in order for it to qualify as the optimal solution.
- **Number of shots:** The previous point leads us to the question of the number of shots required for a calculation. If we seek a precision ϵ in our calculation, VQE requires that we supply $\sim N^4 / \epsilon^2$ number of shots (see Ref. [64], Section 5.1.1). The cost function evaluation in each iteration and for each Hamiltonian term involves cost from number of shots and the number of two-qubit gates for that circuit, which as we saw scales as $\sim N^5$. On the other hand, for QAE, determining the scaling behaviour of the number of shots is highly non-trivial, although it is central to the completion of the scaling analysis. Furthermore, noting that the anneal time

itself scales as the inverse of minimum gap squared (where gap refers to the energy gap between the ground state and the first excited state of the total Hamiltonian, whose final Hamiltonian is the QUBO described in Eq. 4), we require that for annealing to be efficient, the gap must scale polynomially in N . We defer these two important considerations of the anneal time and the number of shots scaling behaviours with system size for a future work, but note that they may favourably or adversely impact the overall scaling of QAE.

3. Embedding

- We now discuss embedding. The number of coefficients to optimize post QAE encoding is $n_{coeff} = d_{CI} \times K$ which results in an n_{coeff} qubit fully connected problem graph. Minor embedding an n_{coeff} qubit all-to-all connected problem requires a physical qubit overhead which in the worst case scales as $\mathcal{O}(n_{coeff}^2)$ [65]. Therefore, the number of physical qubits scale as

$$\text{Number of physical qubits} = \mathcal{O}(N^8 \log^2(N)) \quad (7)$$

In the gate model, the overhead of embedding can be approximately quantified in terms of the additional number of SWAP gates required to account for the limited connectivity between physical qubits. Consider the worst-case scenario of an N qubit quantum circuit where every pair of qubits is connected by a CNOT. Suppose the hardware has only nearest neighbour 1D connectivity, that is, the qubits are arranged as nodes on a path graph (worst case scenario). In this case, the total number of CNOT gates which cannot be executed directly due to connectivity constraints are $\left(\frac{N(N-1)}{2} - N\right)$.

Therefore the total number of SWAP gates incurred, $\mathcal{N}_{\text{additional SWAPs}}$ are bounded by

$$\begin{aligned} & \mathcal{N}_{\text{additional SWAPs}} \\ & \leq \left(\frac{N(N-1)}{2} - N\right) (N-2) \end{aligned} \quad (8)$$

which in the worst case scales as $\mathcal{O}(N^3)$. As a consequence, the overall result fidelity (F_{res}) would degrade by a factor of $\sim F^{\mathcal{N}_{\text{additional SWAPs}}}$ where F denotes the two qubit gate fidelity. This scaling arises from

$$F_{\text{res}} \sim F^{\mathcal{N}_{2\text{qg}} + \mathcal{N}_{\text{additional SWAPs}}} \quad (9)$$

resulting in an exponential decrease of the result fidelity.

- In VQE, although there are gate-based quantum computers to execute the algorithm with over 100 qubits, we are limited by the number of gate operations even for small numbers of physical qubits. On the other hand, in QAE, we are limited by the number of physical qubits. For example, we find that for a given repetition, that is, across hundred λ values that are scanned for our chosen λ range, the number of physical qubits can vary between about 700 to about 900 to construct our QUBO with 80 logical qubits. This also reflects when we wish to increase K in a computation. For example, were we to carry out our computations on H_4 with a split valence basis set such as the 6-31G (4 electron- 5 orbital active space), a QUBO size of 170 (assuming $K = 10$) requires on an average about 4000 physical qubits (over those scanned λ values for which an embedding was found). Finding an embedding with any further increase in K is not possible, since the D-Wave annealers have only 5000 physical qubits. In such cases, one needs to opt for Sub-QUBOs (for example, see Ref. [66]), and additional errors incurred in approximations involved in choice of sub-QUBOs also add to the error budget. It is worth adding that the embedding issue we consider is specific to current state-of-the-art D-Wave hardware and not to the QAE algorithm itself; future advances in this direction, for example, machines with substantially better connectivity, could alleviate embedding-related issues.

4. Net scaling behaviours

Table II summarizes the upper bounds for the individual steps of the QAE and the VQE algorithms (end-to-end). Since the entire analysis is preliminary, we take a simplistic route and assume that the costs can be summed, and thus we pick the highest scaling term for the scaling of an algorithm. We immediately see that the input state preparation step in VQE is exponentially costly (this is not the case for single reference UCC-VQE, since the input state preparation only requires one-qubit gates), and only under the assumption that an oracle supplies the input state does the optimizer step becomes the most steeply scaling. On the other hand, in QAE, embedding is the costliest step. Thus, QAE scales as $N^8 \log_2^2(N)$ and VQE as N^8 per iteration, with the latter assuming the

Table II: Table summarizing the worst case scaling for various steps of the QAE (for determinant-based CISD) and the VQE (for a multi-reference UCC) algorithms. The quantum computing overheads are marked in bold. In the table, N is the total number of spin-orbitals.

Steps	QAE (end-to-end)	VQE (end-to-end)
Hartree-Fock	N^4	N^4
One- and two- electron integrals	N^5	N^5
Evaluation of H_{ij}	N^6	—
Number of CI coefficients	N^4	—
K scaling	$\log_2(N)$	—
$\mathcal{N}_{2\text{qg}}^{\text{iso}}$	—	2^{N^a}
$\mathcal{N}_{2\text{qg}}^{\text{uccsd}}$	—	N^5
Optimizer	—	N^{8b}
Embedding	Num physical qubits (CISD) $\leq N^8 \log_2^2(N)$	Num additional SWAPs $\leq N^3$

^a Under the assumption that the number of determinants grow as $\sim \log(N)$, for an N qubit state for a representative example.

Furthermore, our estimates are based on Qiskit's isometry routine.

^b Cost per iteration for the SLSQP optimizer.

SLSQP optimizer. For comparison, a regular execution of a CCSD or a CISD routine on a traditional computer scales as N^6 . In view of our various simplifications (for instance, VQE: SLSQP is not the optimizer of choice outside statevector type calculations, and QAE: we assume a $\log(\log(2^N))$ behaviour for the growth of number of determinants in N), our finding does not definitely establish the scaling for QAE and VQE, and is to only be viewed as a first step towards a more rigorous scaling analysis for the future. Furthermore, VQE and QAE are both restricted by the current state-of-the-art quantum hardware; even with the current best NISQ computers, it is impractical to go beyond 5000 physical qubits and about 50 two-qubit gates for QAE and VQE executions respectively, and thus we do not expect any advantage anyway over traditional computers for such limited system sizes.

V. CONCLUSION AND FUTURE OUTLOOK

In summary, we have explored the potential of the QAE algorithm as a NISQ tool for carrying out electronic structure calculations by (a) predicting an avoided crossing in the H_4 molecule on a D-Wave quantum computer, and (b) carrying out a preliminary scaling analysis comparison between QAE and the celebrated gate-based VQE algorithm. We anticipate that our analysis would serve as a starting point to bridge a significant gap in literature with regard to the application of quantum annealers to NISQ-era chemistry, in contrast to the extensive body of research dedicated to the gate-based VQE algorithm in the same domain.

We find from our calculations that using the QAE algo-

rithm with 1000 shots and 10 repetitions yields AC with reasonable precision, to within about 20 percent of the reference full configuration interaction values. Furthermore, we find that the result can be substantially improved by increasing the number of shots to 5000, the number of repetitions to 30, and by choosing different anneal times for the ground and excited state energies. The choice of λ range using SAE was found to be sufficient. The improved AC result with 5000 shots and 30 repetitions is to within about 1.2 percent of the FCI value. Among the factors considered, we find that unsurprisingly, the number of shots significantly influences the quality of our results. It is also worth noting at this point that there are several other factors that could be tuned to improve the results further, which we do not carry out in this pilot study. These include, but are not limited to:

- Checking the effect of including more λ values within a chosen λ range.
- Studying the effect of the number of physical qubits that are expended for a computation via embedding.
- Our calculations are spread over a time period of about three months, and thus we expect that our results and analyses would have errors due to drift in machine parameters. It is, however, well beyond the scope of the current study to address the issue.

Via our scaling analysis, where we estimate costs for each step of the QAE and the VQE algorithms starting from problem inputs (HF, common to QAE and VQE), AO to MO integral transformation (common), CISD Hamiltonian matrix elements evaluation (specific to QAE), encoding the functional in its QUBO form

(QAE), and input reference state isometry (VQE)) and then moving to the main processing steps (parameter update (VQE), convergence (VQE), number of two-qubit gates in the UCCSD ansatz circuit (VQE), embedding (VQE and QAE)), we find that performing CI calculations using QAE is a compelling NISQ-era contender for quantum chemistry on current-day quantum computers. Although both QAE and VQE scale worse relative to established classical methods (even under the strong assumption that an oracle supplies the input state for VQE), we find that they scale comparably between each other (it is also important to add that on grounds of the problem being very non-trivial, we do not estimate the scaling of the anneal time and number of required shots itself in QAE). We add that our conclusion comes with two caveats: (a) our analysis is to be seen as preliminary with scope for further refinement, and (b) we do not consider variants of VQE or QAE but rather their vanilla versions. Our hardware results indicate that in order to use the VQE algorithm to predict energies accurately within a considered active space, one requires quantum devices with gate fidelities well beyond the current best capabilities. On the other hand, the QAE algorithm is well-placed to obtain energies with reasonable precision on current-day D-Wave hardware. However, the next natural step of studying the effect of D-Wave hardware errors as we scale up the size of the molecular systems would require more physical qubits, in view of the embedding overheads. An alternative that has not been explored in this work is the use of sub-QUBOs to extend the calculations to larger system sizes in current D-Wave computers.

We anticipate that our study paves way for more comprehensive and detailed studies on the underexplored QAE algorithm, and also for algorithmic advances in NISQ approaches for quantum chemistry in the quantum

annealing framework.

ACKNOWLEDGMENTS

This work was supported by the European Commission EIC-Transition project RoCCQeT (GA 101112839). VSP acknowledges support from CRG grant (CRG/2023/002558) for some of the computations. AAZ and VSP sincerely acknowledge Palak Chawla for her tremendous support and patience in helping us with the VQE computations, and Disha Shetty for patiently reading the initial drafts and giving her feedback, which in turn helped improve the quality of the manuscript. VSP and AAZ acknowledge Prof. Bhanu Pratap Das for discussions on QAE and support with D-Wave time, and Prof. Debashis Mukherjee for discussions on the general nature of AC. The authors acknowledge Mr. Jose Miralles for fruitful discussions on Sub-QUBOs. KS acknowledges support from Quantum Leap Flagship Program (Grant No. JPMXS0120319794) from the MEXT, Japan, Center of Innovations for Sustainable Quantum AI (JPMJPF2221) from JST, Japan, and Grants-in-Aid for Scientific Research C (21K03407) and for Transformative Research Area B (23H03819) from JSPS, Japan. J.N and J.R thankfully acknowledge RES resources provided by Barcelona Supercomputing Center in Marenostrom 5 to FI-2025-1-0043.

VI. DATA AVAILABILITY

All the data is included in the article. The details of our code will be available on reasonable request.

-
- [1] A. Peruzzo *et al.*, Nat. Commun. **5**, 4213 (2014).
 - [2] A. Kandala, A. Mezzacapo, K. Temme, M. Takita, M. Brink, J. M. Chow, and J. M. Gambetta, Nature **549**, 242 (2017).
 - [3] F. Arute *et al.*, Science **369**, 1084 (2020).
 - [4] Y. Nam *et al.*, npj Quantum Inf. **6**, 33 (2020).
 - [5] C. Ying *et al.*, Phys. Rev. Lett. **130**, 110601 (2023).
 - [6] K. Sugisaki, T. Kato, Y. Minato, K. Okuwaki, and Y. Mochizuki, Phys. Chem. Chem. Phys. **24**, 8439 (2022).
 - [7] S. Guo *et al.*, Nat. Phys. **20**, 1240 (2024).
 - [8] M. Ostaszewski, E. Grant, and M. Benedetti, Quantum **5**, 391 (2021).
 - [9] H. L. Tang, V. Shkolnikov, G. S. Barron, H. R. Grimsley, N. J. Mayhall, E. Barnes, and S. E. Economou, PRX Quantum **2**, 020310 (2021).
 - [10] R. Villela, V. S. Prasanna, and B. P. Das, Eur. Phys. J. Plus **137**, 1017 (2022).
 - [11] K. Sugisaki, K. Toyota, K. Sato, D. Shiomi, and T. Takui, J. Phys. Chem. Lett. **12**, 2880 (2021).
 - [12] Sumeet, S. Prasanna V, B. P. Das, and B. K. Sahoo, Quantum Rep. **4**, 173 (2022).
 - [13] K. Bharti *et al.*, Rev. Mod. Phys. **94**, 015004 (2022).
 - [14] M. Motta and J. E. Rice, Wiley Interdiscip. Rev. Comput. Mol. Sci. **12**, e1580 (2022).
 - [15] P. Chawla *et al.*, Phys. Rev. A **111**, 022817 (2025).
 - [16] A. Teplukhin, B. K. Kendrick, and D. Babikov, J. Chem. Theory Comput. **15**, 4555 (2019).

- [17] V. Kumar, N. Baskaran, V. S. Prasanna, K. Sugisaki, D. Mukherjee, K. G. Dyall, and B. P. Das, *Phys. Rev. A* **109**, 042808 (2024).
- [18] A. Teplukhin, B. K. Kendrick, and D. Babikov, *Phys. Chem. Chem. Phys.* **22**, 26136 (2020).
- [19] A. Teplukhin, B. K. Kendrick, S. Tretiak, and P. A. Dub, *Sci. Rep.* **10**, 20753 (2020).
- [20] A. Teplukhin *et al.*, *Sci. Rep.* **11**, 18796 (2021).
- [21] M. Illa and M. J. Savage, *Phys. Rev. A* **106**, 052605 (2022).
- [22] S. A. Rahman, R. Lewis, E. Mendicelli, and S. Powell, *Phys. Rev. D* **104**, 034501 (2020).
- [23] K. Sugisaki, T. Kato, Y. Minato, K. Okuwaki, and Y. Mochizuki, *Phys. Chem. Chem. Phys.* **24**, 8439 (2022).
- [24] D. Halder, V. S. Prasanna, and R. Maitra, *J. Chem. Phys.* **157**, 174117 (2022).
- [25] D. Halder, V. S. Prasanna, V. Agarawal, and R. Maitra, *Int. J. Quantum Chem.* **123**, e27021 (2023).
- [26] I. O. Sokolov, P. K. Barkoutsos, P. J. Ollitrault, D. Greenberg, J. Rice, M. Pistoia, and I. Tavernelli, *J. Chem. Phys.* **152**, 124107 (2020).
- [27] F. Pavosevic, I. Tavernelli, and A. Rubio, *J. Phys. Chem. Lett.* **14**, 7876 (2023).
- [28] M. Rossmannek, F. Pavosevic, A. Rubio, and I. Tavernelli, *J. Phys. Chem. Lett.* **14**, 3491 (2023).
- [29] R. Xia, T. Bian, and S. Kais, *J. Phys. Chem. B* **122**, 3384 (2018).
- [30] M. Streif, F. Neukart, and M. Leib, *Quantum Technology and Optimization Problems QTOP 2019* **11413** (2019).
- [31] I. G. Ryabinkin, T. C. Yen, S. N. Genin, and A. Izmaylov, *J. Chem. Theory Comput.* **14**, 6317 (2018).
- [32] S. N. Genin, I. G. Ryabinkin, and A. F. Izmaylov, *arXiv:1901.04715* (2019).
- [33] J. Copenhaver, A. Wasserman, and B. W. Kaufmann, *J. Chem. Phys.* **154**, 034105 (2021).
- [34] J. Paldus, P. Piecuch, L. Pylypow, and B. Jeziorski, *Phys. Rev. A* **47**, 2738 (1993).
- [35] G. M. J. Barca *et al.*, *J. Chem. Phys.* **152**, 154102 (2022).
- [36] T. Kadowaki and H. Nishimori, *Phys. Rev. E* **58**, 5355 (1998).
- [37] T. Kadowaki, *arXiv preprint quant-ph/0205020* (2002).
- [38] E. Farhi, J. Goldstone, S. Gutmann, and M. Sipser, *arXiv preprint quant-ph/0001106* (2000).
- [39] Fan, P. Dong, and P. Piecuch, *Adv. Quantum Chem.* **51**, 1 (2015).
- [40] J. Hubbard, *Math. Phys. Sci.* **276**, 238 (1963).
- [41] J. Dukelsky, G. Dussel, J. G. Hirsch, and P. Schuck, *Nucl. Phys. A* **714**, 63 (2003).
- [42] T. Henderson, J. Dukelsky, E. Gustavo, A. Signoracci, and T. Duguet, *Phys. Rev. C* **89**, 63 (2014).
- [43] J. von Neumann and E. P. Wigner, *Phys. Z* **30** (1929).
- [44] *dwavesystems, dwave-samplers* (2024), accessed: 2024-12-12.
- [45] K. Boothby, P. Bunyk, J. Raymond, and A. Roy, *Next-generation topology of D-wave quantum processors* (2020), *arXiv:2003.00133*.
- [46] M. Hanauer and A. Kohn, *J. Chem. Phys.* **134**, 204111 (2011).
- [47] M. Treinish *et al.*, *Qiskit: An open-source framework for quantum computing* (2022).
- [48] S. Sivarajah, S. Dilkes, A. Cowtan, W. Simmons, A. Edgington, and R. Duncan, *Quantum Sci. Technol.* **6**, 014003 (2020).
- [49] A. Kissinger and J. van de Wetering, in *Proceedings 16th International Conference on Quantum Physics and Logic*, Chapman University, Orange, CA, USA., 10-14 June 2019, *Electronic Proceedings in Theoretical Computer Science*, Vol. 318, edited by B. Coecke and M. Leifer (Open Publishing Association, 2020) pp. 229–241.
- [50] J. Riu, J. Nogué, G. Vilaplana, A. Garcia-Saez, and M. P. Estarellas, *Reinforcement learning based quantum circuit optimization via ZX-calculus* (2024), *arXiv:2312.11597 [quant-ph]*.
- [51] P. Chawla, D. Shetty, P. B. Tsemo, K. Sugisaki, J. Riu, J. Nogué, D. Mukherjee, and V. S. Prasanna, *VQE calculations on a NISQ era trapped ion quantum computer using a multireference unitary coupled cluster ansatz: application to the BeH₂ insertion problem* (2025), *arXiv:2504.07037*.
- [52] I. Shavitt, *Essentials of computational chemistry pp. 237* (Wiley, 1961).
- [53] D. W. Berry, C. Gidney, M. Motta, J. R. McClean, and R. Babbush, *Quantum* **3**, 208 (2019).
- [54] V. von Burg, G. H. Low, T. Haner, D. S. Steiger, M. Reiher, M. Roetteler, and M. Troyer, *Phys. Rev. Res.* **3**, 033055 (2021).
- [55] J. Lee, D. W. Berry, C. Gidney, W. J. Huggins, J. R. McClean, N. Wiebe, and R. Babbush, *PRX Quantum* **2**, 030305 (2021).
- [56] I. Shavitt, *Mathematical Frontiers in Computational Chemical Physics in D. G. Truhlar ed. pp. 300-349* (Springer, New York, 1988).
- [57] I. Shavitt, *The Unitary Group (Lecture Notes in Chemistry No. 22 in J. Hinze, ed. pp. 51-99* (Springer, Berlin, 1988).
- [58] R. Iten, R. Colbeck, I. Kukuljan, J. Home, and M. Christandl, *Phys. Rev. A* **93**, 032318 (2016).
- [59] V. V. Shende, S. S. Bullock, and I. L. Markov, *IEEE Trans. on Computer-Aided Design* **25(6)**, 1000 (2006).
- [60] K. Sugisaki, S. Nakazawa, K. Toyota, K. Sato, D. Shiomi, and T. Takui, *ACS. Cent. Sci.* **5**, 167 (2019).
- [61] Y. Ino, M. Yonekawa, H. Yuzawa, Y. Minato, and K. Sugisaki, *Phys. Chem. Chem. Phys.* **26**, 30044 (2024).
- [62] M. Larocca, S. Thanasilp, S. Wang, K. Sharma, J. Biamente, P. J. Coles, L. Cincio, J. R. McClean, Z. Holmes, and M. Cerezo, *Nat. Rev. Phys.* **7**, 174 (2025).
- [63] D. Kraft, *A software package for sequential quadratic programming*, Technical Report DFVLR-FR 88-28 (Deutsche Forschungs- und Versuchsanstalt für Luft- und Raumfahrt (DFVLR), 1988).
- [64] J. Tilly, H. Chen, S. Cao, D. Picozzi, K. Setia, Y. Li, E. Grant, L. Wossnig, I. Runger, G. H. Booth, and J. Tennyson, *Phys. Rep.* **986**, 1 (2022).

- [65] A. Palacios, A. Garcia-Saez, B. Julia-Diaz, and M. P. Estarellas, Phys. Rev. Appl. **23**, 054070 (2025).
 [66] Y. Atobe, M. Tawada, and N. Togawa, IEEE Transactions on Computers **71**, 2606 (2022).

Appendix A: Derivation of fidelity bounds

The energy of a quantum state $|\Psi\rangle$ is given by

$$E = \langle \Psi | H | \Psi \rangle. \quad (\text{A1})$$

Substituting the Hamiltonian, H , with its spectral decomposition, we obtain

$$\begin{aligned} E &= \sum_{n=0}^{d-1} E_n p_n \\ &= E_0 p_0 + \sum_{n=1}^{d-1} E_n p_n, \end{aligned} \quad (\text{A2})$$

where E_n is the energy of the eigenstate $|E_n\rangle$, and $p_n = |\langle E_n | \Psi \rangle|^2$ represents its population.

Since the eigenvalues, E_n , are ordered in increasing magnitude, any energy, E_n , with $n \in 1, \dots, d-1$, satisfies the bounds:

$$E_1 \leq E_n \leq E_{max}, \quad (\text{A3})$$

where $E_{max} = E_{d-1}$ denotes the largest eigenvalue of H .

Thus, the second term in the right hand side of Eq. (A2) is bounded as

$$E_1(1 - p_0) \leq \sum_{n=1}^{d-1} E_n p_n \leq E_{max}(1 - p_0), \quad (\text{A4})$$

where we have used the normalization condition $\sum_{n=1}^{d-1} p_n = 1 - p_0$. Substituting this bound into Eq. (A2), the energy of the state $|\Psi\rangle$ is bounded by

$$E_0 p_0 + E_1(1 - p_0) \leq E \leq E_0 p_0 + E_{max}(1 - p_0). \quad (\text{A5})$$

After some algebra and identifying $p_0 = |\langle E_0 | \Psi \rangle|^2 = \mathcal{F}$ as the fidelity of $|\Psi\rangle$ with the ground state, we derive the following bounds for the fidelity:

$$1 - \frac{E - E_0}{E_1 - E_0} \leq \mathcal{F} \leq 1 - \frac{E - E_0}{E_{max} - E_0}. \quad (\text{A6})$$

In our case, we check if the bounds are satisfied for the case of our avoided crossing problem for H_4 in square geometry where $E_0 = E_g$, $E_1 = E_e$ and $E = E_{g, QAE}$.

The lower bound represents the case where the population outside the ground state is entirely in the first excited state, the one with the lowest energy. On the other hand, the upper bound corresponds to the scenario where all the population outside the ground state is in the state with the highest energy. In any realistic situation, the true population distribution will lie somewhere between these two extremes.

Appendix B: Cost of evaluating CISD Hamiltonian matrix elements

Here, we present the cost of generating the CISD Hamiltonian matrix elements, $\langle \Phi_m | H | \Phi_n \rangle$, which are fed as inputs to QAE. The cost is analysed by categorizing the matrix elements into 4 patterns and applying the Slater–Condon rules. We begin by classifying $\langle \Phi_m | H | \Phi_n \rangle$:

- Pattern 1: $|\Psi_m\rangle = |\Psi_n\rangle$ (diagonal element of the CI matrix), for which the cost of evaluating the matrix element goes as $\mathcal{O}(N^2)$.
- Pattern 2: $|\Phi_m\rangle$ and $|\Phi_n\rangle$ have two different occupation indices (for example, $|\Phi_m\rangle = |\Phi_i^a\rangle$ and $|\Phi_n\rangle = |\Phi_i^b\rangle$). The cost of evaluating $\langle \Phi_m | H | \Phi_n \rangle$ then scales as $\mathcal{O}(N)$.
- Pattern 3: $|\Psi_m\rangle$ and $|\Psi_n\rangle$ have four different occupation indices (for instance, $|\Phi_m\rangle = |\Phi_i^a\rangle$ and $|\Phi_n\rangle = |\Phi_{ij}^{bc}\rangle$). The cost of evaluating $\langle \Phi_m | H | \Phi_n \rangle$ then scales as $\mathcal{O}(1)$.
- Pattern 4: $|\Psi_m\rangle$ and $|\Psi_n\rangle$ have more than four differing occupation indices (for instance, $|\Phi_m\rangle = |\Phi_i^a\rangle$ and $|\Phi_n\rangle = |\Phi_{jk}^{bc}\rangle$). These matrix elements are zero due to the Slater–Condon rules.

From the table, we see that the cost of evaluating the matrix elements for determinant-based CISD is at most N^6 . We comment on why the scaling of serial number 5 is not $\mathcal{O}(N^2) \times \mathcal{O}(N^2) \times \mathcal{O}(N) = \mathcal{O}(N^5)$. This is because one of the indices of $|\Phi_m\rangle = |\Phi_j^b\rangle$ is fixed to either $j = i$ or $a = b$. Thus, the number of possible $|\Phi_n\rangle$ scales as ${}^2C_1 \times \mathcal{O}(N) = \mathcal{O}(N)$. Similarly, for serial number 11, the scaling is not $\mathcal{O}(N^4) \times \mathcal{O}(N^4) \times \mathcal{O}(N) = \mathcal{O}(N^9)$, because three out of four indices of $|\Phi_n\rangle$ should be fixed, and the number of possible $|\Phi_n\rangle$ scales as ${}^4C_3 \times \mathcal{O}(N) = \mathcal{O}(N)$.

In the case of GUGA-based CISD, we want to know the cost scaling for evaluating $\langle \Phi_m | H | \Phi_n \rangle$, where $|\Phi_m\rangle$ and

Table III: Table showing worst-case scaling for the cost of computing different CISD Hamiltonian matrix elements. In the table, (p, q, r, \dots) refer to general indices, (i, j, k, \dots) refer to indices of occupied spin orbitals, and (a, b, c, \dots) refer to indices of unoccupied spin orbitals.

S. No.	$ \Phi_m\rangle$	$ \Phi_n\rangle$	# same indices	Examples of $ \Phi_n\rangle$	Pattern	Scaling
1.	$ 0\rangle$	$ 0\rangle$	0	$ 0\rangle$	1	$\mathcal{O}(1) \times \mathcal{O}(1) \times \mathcal{O}(N^2) = \mathcal{O}(N^2)$
2.	$ 0\rangle$	$ S\rangle$	0	$ \Phi_i^a\rangle$	2	$\mathcal{O}(1) \times \mathcal{O}(N^2) \times \mathcal{O}(N) = \mathcal{O}(N^3)$
3.	$ 0\rangle$	$ D\rangle$	0	$ \Phi_{ij}^{ab}\rangle$	3	$\mathcal{O}(1) \times \mathcal{O}(N^4) \times \mathcal{O}(1) = \mathcal{O}(N^4)$
4.	$ \Phi_i^a\rangle$	$ S\rangle$	2	$ \Phi_i^a\rangle$	1	$\mathcal{O}(N^2) \times \mathcal{O}(1) \times \mathcal{O}(N^2) = \mathcal{O}(N^4)$
5.	$ \Phi_i^a\rangle$	$ S\rangle$	1	$ \Phi_i^b\rangle, \Phi_j^a\rangle$	2	$\mathcal{O}(N^2) \times \mathcal{O}(N) \times \mathcal{O}(N) = \mathcal{O}(N^5)$
6.	$ \Phi_i^a\rangle$	$ S\rangle$	0	$ \Phi_j^b\rangle$	3	$\mathcal{O}(N^2) \times \mathcal{O}(N^2) \times \mathcal{O}(1) = \mathcal{O}(N^4)$
7.	$ \Phi_i^a\rangle$	$ D\rangle$	2	$ \Phi_{ij}^{ab}\rangle, \Phi_{ij}^{ba}\rangle$	2	$\mathcal{O}(N^2) \times \mathcal{O}(N^2) \times \mathcal{O}(N) = \mathcal{O}(N^5)$
8.	$ \Phi_i^a\rangle$	$ D\rangle$	1	$ \Phi_{ij}^{bc}\rangle, \Phi_{jk}^{ab}\rangle$	3	$\mathcal{O}(N^2) \times \mathcal{O}(N^3) \times \mathcal{O}(1) = \mathcal{O}(N^5)$
9.	$ \Phi_i^a\rangle$	$ D\rangle$	0	$ \Phi_{jk}^{bc}\rangle$	4	-
10.	$ \Phi_{ij}^{ab}\rangle$	$ D\rangle$	4	$ \Phi_{ij}^{ab}\rangle$	1	$\mathcal{O}(N^4) \times \mathcal{O}(1) \times \mathcal{O}(N^2) = \mathcal{O}(N^6)$
11.	$ \Phi_{ij}^{ab}\rangle$	$ D\rangle$	3	$ \Phi_{ik}^{ab}\rangle, \Phi_{kj}^{ab}\rangle, \Phi_{ij}^{ac}\rangle, \Phi_{ij}^{cb}\rangle, \dots$	2	$\mathcal{O}(N^4) \times \mathcal{O}(N) \times \mathcal{O}(N) = \mathcal{O}(N^6)$
12.	$ \Phi_{ij}^{ab}\rangle$	$ D\rangle$	2	$ \Phi_{ij}^{cd}\rangle, \Phi_{ik}^{ac}\rangle, \Phi_{kj}^{ac}\rangle, \Phi_{kj}^{cb}\rangle, \dots$	3	$\mathcal{O}(N^4) \times \mathcal{O}(N^2) \times \mathcal{O}(1) = \mathcal{O}(N^6)$
13.	$ \Phi_{ij}^{ab}\rangle$	$ D\rangle$	1	$ \Phi_{ik}^{ab}\rangle, \Phi_{ik}^{cd}\rangle, \Phi_{kl}^{cb}\rangle, \Phi_{kl}^{ac}\rangle, \dots$	4	-
14.	$ \Phi_{ij}^{ab}\rangle$	$ D\rangle$	0	$ \Phi_{kl}^{cd}\rangle$	4	-

$|\Phi_n\rangle$ are symmetry-adapted CSFs. The scaling behavior of the matrix elements evaluation is very similar to that of determinant-based one. However, in the GUGA-CI approach, we incur extra cost for evaluating an additional coefficient depending on the pathways of Shavitt graph, with the cost for this step possibly scaling as $\mathcal{O}(N)$.

Appendix C: Details of input state preparation: a representative example

Here, we present the details of the conditions under which our representative example yielded the 2^N scaling for the number of two-qubit gates for the isometry associated with input state preparation for VQE. We consider a simplified model of a two-electron system where the number of determinants in the wavefunction grow as $\log(\log(2^N))$. Below we explicitly report the dominant excitations considered along with their respective coefficients (chosen to be ≤ 0.721). The choice of determinants is based on excitations that remain close to the valence (occupied) orbitals. The determinants are reported using interleaved notation where occupancies are represented as $(\alpha, \beta, \alpha, \beta, \dots)$:

- For $N = 4$:

$$|\Psi\rangle = 0.70|1100\rangle + 0.71|0011\rangle.$$

- For $N = 6$:

$$|\Psi\rangle = 0.60|110000\rangle - 0.6|001100\rangle + 0.529|000011\rangle.$$

- For $N = 8$:

$$|\Psi\rangle = 0.60|11000000\rangle - 0.6|00110000\rangle + 0.529|00001100\rangle.$$

- For $N = 10$:

$$|\Psi\rangle = 0.72|1100000000\rangle - 0.6|0011000000\rangle + 0.245|0000110000\rangle - 0.245|1001000000\rangle.$$

- For $N = 12$:

$$|\Psi\rangle = 0.72|110000000000\rangle - 0.6|001100000000\rangle + 0.245|100100000000\rangle - 0.245|011000000000\rangle.$$

- For $N = 14$:

$$|\Psi\rangle = 0.72|11000000000000\rangle - 0.6|00110000000000\rangle + 0.245|10010000000000\rangle - 0.245|01100000000000\rangle.$$

- For $N = 16$:

$$|\Psi\rangle = 0.72|1100000000000000\rangle - 0.6|0011000000000000\rangle + 0.245|1001000000000000\rangle - 0.245|0110000000000000\rangle.$$